

## Thermal development of microstructure and precipitation effects in Mg–10wt%Gd alloy

Jakub Čížek\*, Ivan Procházka, Bohumil Smola, Ivana Stulíková, Radomír Kužel, Zdeněk Matěj, and Viktoria Cherkaska

Charles University, Faculty of Mathematics and Physics, V Holešovičkách 2, 180 00 Prague 8, Czech Republic

Received 15 April 2005, revised 5 December 2005, accepted 22 December 2005

Published online 13 February 2006

PACS 61.10.Nz, 61.72.Ji, 61.72.Qq, 78.70.Bj

Thermal effects on the microstructure and precipitation in Mg–10wt%Gd alloy were studied in this work. The role of lattice defects was investigated using positron annihilation spectroscopy. Studies of defects by positron annihilation were combined with X-ray diffraction and microhardness measurements. Vacancies bound to Gd atoms were found in the homogenised sample quenched down to room temperature. Subsequently, clustering of Gd atoms takes place with increasing temperature. The Gd-rich clusters represent precursors for further precipitates of the  $\beta''$  phase. The formation of fine  $\beta''$  phase particles leads to a maximum in the hardness. Vacancy-like misfit defects are introduced by precipitation of  $\beta'$  phase particles in the sample annealed to higher temperatures. A good correlation between the intensity of trapped positrons and the contribution by positrons annihilating Gd electrons was found.

© 2006 WILEY-VCH Verlag GmbH & Co. KGaA, Weinheim

### 1 Introduction

Lightweight Mg-based alloys enable a significant weight reduction to be made, which is particularly important in automotive or aeronautical applications. However, use of conventional Mg-based alloys is limited due to a loss of their mechanical properties at elevated temperatures. Improved mechanical properties, however, even at temperatures above 300 °C, can be achieved using non-traditional alloying elements, in particular rare earths [1]. The Mg–Gd system is one of the candidates for novel Mg-based hardenable alloys with high creep resistance at elevated temperatures. Solubility of Gd in Mg is relatively high but it decreases significantly with decreasing temperature [2]. It enables remarkable precipitation hardening to be achieved during the decomposition of supersaturated solid solution [3]. The change in microstructure of solution treated Mg–Gd alloys with increasing temperature was investigated in [4] using electrical resistivity measurements combined with TEM. It was found that the  $\alpha'$ -Mg supersaturated solid solution decomposes with increasing temperature into the following successive phases:  $\beta''$  ( $D0_{19}$ ) metastable  $\rightarrow$   $\beta'$  ( $c$ -bco) metastable  $\rightarrow$   $\beta$  (fcc) stable. Note that  $\beta'$  phase developed in Mg–15%Gd but could not be detected in Mg–Gd alloys with a lower content of Gd [4]. The  $\beta''$  phase particles are fully coherent with the Mg matrix; the coherence is lost in some interfaces in the case of  $\beta'$  phase precipitates, and the  $\beta$  phase particles are completely incoherent in the matrix. Thus, the formation of semicoherent and incoherent precipitates is accompanied by the introduction of open volume misfit defects in the interfaces where the coherence was lost. Moreover, the precipitation effects in Mg–Gd alloys are caused by the long-range vacancy-assisted diffusion of Gd atoms. Hence, it is clear that lattice defects play an important role in the decomposition of a supersaturated solid solution and also precipita-

\* Corresponding author: e-mail: Jakub.Cizek@mff.cuni.cz, Phone: +420221911288, Fax: +420221912567

tion effects. In the present work we carried out defect studies of a solution treated Mg–9.33wt%Gd (Mg10Gd) alloy subjected to a subsequent isochronal anneal. The change in microstructure with increasing temperature was investigated in particular with respect to variations of defect types and densities. The defect studies used positron annihilation spectroscopy (PAS), which is a well established non-destructive technique with a very high sensitivity to open volume defects such as vacancies, vacancy clusters, dislocations etc. [5]. Two complementary techniques of PAS were employed in the present work, namely: (i) positron lifetime (PL) spectroscopy [6], which enables one to identify defect types and to determine defect densities, and (ii) coincidence Doppler broadening (CDB) measurements [7], which are sensitive to local chemical environment of defects. PAS data were combined with X-ray diffraction (XRD) and microhardness measurements. The isochronal annealing of the alloy studied was performed exactly in the same way as that used in [4]. It enables our results with electrical resistivity and TEM data obtained in [4] to be compared directly.

## 2 Experimental details

The Mg10Gd alloy was prepared from technical purity Mg by squeeze casting. In this paper the concentration of Gd is given in weight percent. The as-cast material was homogenised by annealing at 500 °C for 6 hours and then quenched in water at room temperature. After microstructural characterisation of the as-quenched state, the sample was subjected to step-by-step isochronal annealing with an effective heating rate 1 K/min, i.e. analogous to [4]. Annealing was carried out in a silicon oil bath up to 250 °C and above that in a vertical furnace with a protective Ar atmosphere. Each annealing step was followed by rapid quenching into water at room temperature. Subsequent microstructural investigations were undertaken at room temperature.

In addition, reference specimens of technical purity Mg (99.5%), high purity Mg (99.95%) and high purity Gd (99.9%) were studied. The reference specimens were annealed at 280 °C for 30 min and at 850 °C for 1 h in the case of Mg and Gd, respectively, in order to remove virtually all the existing defects. In addition, one sample of technical purity Mg was cold rolled at room temperature with a thickness reduction of  $\varepsilon = 40\%$ .

A  $^{22}\text{Na}$  positron source of activity of 1.5 MBq sealed between two 2  $\mu\text{m}$  thick mylar foils was used for the PAS measurements. The diameter of the positron source spot was  $\approx 3$  mm.

A fast–fast PL spectrometer, similar to that described in [8, 9], was employed in the present work. The time resolution of the spectrometer was 170 ps (FWHM) for  $^{22}\text{Na}$  at a typical coincidence counting rate of 120  $\text{s}^{-1}$ . At least  $10^7$  counts were collected in each PL spectrum. Measured PL spectra were analysed using a maximum-likelihood procedure [10]. The CDB spectrometer consisted of two high purity germanium (HPGe) detectors and a commercial nuclear instrument module (NIM) operated by a PC. The energy resolution of the spectrometer was 1.1 keV (FWHM) at 511 keV energy and the coincidence count rate was  $\approx 650$   $\text{s}^{-1}$ . At least  $10^8$  events were collected in each two-dimensional CDB spectrum, which was subsequently reduced to a one-dimensional Doppler profile with a reduction in resolution. In order to determine the nature of positron annihilation sites, relative changes of Doppler profiles were followed as ratios of the profiles normalized to equal area to those of a proper reference profile normalized to the same area. The CDB profiles were made symmetrical with respect to the origin and only the parts corresponding to positive Doppler shifts are shown. The reference profile was chosen to be “well annealed (defect-free) Mg (technical purity)”.

Positron lifetimes for defect-free materials and various defect configurations were calculated using the so-called atomic superposition (ATSUP) method [11, 12]. In our calculations the correlation part of the positron potential was determined using the parametrization obtained by Boroński and Nieminen [13] within the framework of the local-density approximation for positrons. A vacancy is created simply by removing one atom from a supercell used in the calculations. We used a 500 atom supercell for Mg and Gd and a 1000 atom supercell for the Mg10Gd alloy. In order to model a substitutional solid solution 17 randomly selected Mg atoms in a 1000 atom supercell were replaced by Gd atoms.

TEM observations of the microstructure were undertaken on a JEOL 2000 FX electron microscope operating at 200 kV with an EDX system LINK AN 10000. Thin foils for TEM were electropolished in a twin-jet device TENUPOL 2. X-ray studies were carried out with the aid of XRD7 and HZG4 (Seifert-FPM) powder diffractometers. Cu  $K_{\alpha}$  radiation, filtered with a nickel foil was used with Soller slits placed in the diffracted beam. The Vickers microhardness was measured using a LECO microtester with an applied load of 100 g for 10 s.

### 3 Results and discussion

#### 3.1 References specimens

Experimental PL results for well-annealed pure Mg and Gd reference specimens are shown in Table 1. All well annealed reference specimens exhibit a single component PL spectrum (except of the source contribution) with lifetime  $\tau_1$ . The calculated bulk positron lifetimes  $\tau_B$ , i.e. lifetimes of free positrons in defect-free material, for Mg and Gd are given in Table 2. Clearly, there is a reasonable agreement between the experimental lifetime  $\tau_1$  and the corresponding calculated bulk lifetime  $\tau_B$  for all well annealed reference specimens. Moreover, the experimental lifetimes  $\tau_1$  obtained on the well annealed Mg samples agree very well with the bulk Mg lifetime measured in [14]. Thus, the well annealed specimens can be regarded as “defect-free” materials because they exhibit a very low density of defects and virtually all positrons annihilate from the free state. It is clear from Table 1 that there is only a very slight difference in the PL results for high purity Mg (99.95%) and technical purity Mg (99.5%) specimens. Similarly, virtually no difference between these two Mg specimens was detected by CDB. It indicates that the impurities present in the technical purity grade Mg have no influence on the PAS results.

In order to obtain information on the lifetime of positrons trapped at dislocations in Mg we measured a cold rolled Mg specimen (technical purity, thickness reduction  $\varepsilon = 40\%$ ). The cold rolled specimen exhibits a two component PL spectrum, see Table 1. The shorter component comes from free positrons while the longer one with a lifetime of  $\tau_2 = 256$  ps represents the contribution of positrons trapped at the dislocations. It should be noted that it is generally accepted that a dislocation line is only a shallow positron trap. Once a positron is trapped at a dislocation line, it diffuses quickly along it (pipe diffusion) and becomes eventually trapped at a vacancy anchored in the elastic field of the dislocation [15]. The free volume of a vacancy bound to a dislocation is slightly reduced because it is squeezed by the elastic field

**Table 1** Experimental lifetimes  $\tau_1$ ,  $\tau_2$  and corresponding relative intensities  $I_1$ ,  $I_2$  of the exponential components resolved in PL spectra of studied samples. The quantity  $\tau_f^{STM}$  calculated using the STM from Eq. (2) is given in the last column.

specimen	$\tau_1$ (ps)	$I_1$ (%)	$\tau_2$ (ps)	$I_2$ (%)	$\tau_f^{STM}$ (ps)
Gd 99.9%					
well annealed (850 °C/1 h)	201.3 ± 0.5	100	–	–	–
Mg 99.95%					
well annealed 280 °C/30 min	225.3 ± 0.4	100	–	–	–
Mg 99.5%					
well annealed 280 °C/30 min	224.9 ± 0.5	100	–	–	–
Mg 99.5%					
cold rolled $\varepsilon = 40\%$	160 ± 10	14 ± 4	256 ± 2	86 ± 1	236 ± 3
Mg10Gd as quenched	194 ± 5	63 ± 2	305 ± 9	37 ± 2	224 ± 1

**Table 2** Calculated bulk lifetimes  $\tau_B$  of free positrons in defect-free material and lifetimes  $\tau_v$  of positrons trapped in vacancy. For the Mg10Gd alloy we calculated the lifetime of positrons trapped at (i) a vacancy surrounded by Mg atoms as the nearest neighbours (denoted by superscript <sup>a</sup>) and (ii) a vacancy–Gd pair, i.e. a vacancy with one Gd atom in the nearest neighbour position (denoted by superscript <sup>b</sup>). The calculations were performed by the ATSUP technique.

material	$\tau_B$ (ps)	$\tau_v$ (ps)
Gd	204	311
Mg	233	299
Mg10Gd	234	300 <sup>a</sup> 294 <sup>b</sup>

of the dislocation. Thus, as a rule the lifetimes of positrons trapped at dislocations in metals are about of several tens ps shorter than the monovacancy lifetime in the same metal. The calculated lifetimes  $\tau_v$  for positrons trapped at a monovacancy in Mg and Gd are listed in the last column of Table 1. Using the two-state trapping model [6] one can calculate dislocation density  $\rho$  in the deformed sample

$$\rho_D = \frac{1}{v_D} \frac{I_2}{I_1} \left( \frac{1}{\tau_B} - \frac{1}{\tau_2} \right), \quad (1)$$

where  $v_D$  denotes the specific positron trapping rate for Mg-dislocation. Using the value  $v_D = 1 \times 10^{-4} \text{ s}^{-1} \text{ m}^2$  obtained from [16] assuming dislocations with the burgers vector  $\mathbf{b} = \frac{1}{3} a [2 \bar{1} \bar{1} 0]$ , we obtained  $\rho_D = 3 \times 10^{13} \text{ m}^{-2}$  for the deformed Mg sample. In the frame of STM the quantity

$$\tau_f^{\text{STM}} = \left( \frac{I_1}{\tau_1} + \frac{I_2}{\tau_2} \right)^{-1} \quad (2)$$

equals the bulk positron lifetime  $\tau_B$  [6]. The relation (2) is often used to check if the assumptions of the two-state STM are satisfied. In our case the assumptions mean that we have a single type of defects (dislocations), the dislocations are distributed homogeneously, and there is no detrapping of positrons once trapped at dislocations. The quantity  $\tau_f^{\text{STM}}$  calculated from Eq. (2) for cold rolled Mg is shown in the last column of Table 1. It is clear that  $\tau_f^{\text{STM}}$  is slightly higher than  $\tau_B$ . It is most probably because of non-homogeneously distributed dislocations. It was shown that pile-up of dislocations in the vicinity of grain boundaries leads to deviations from STM [17]. Nevertheless, the  $\tau_f^{\text{STM}}$  does not differ from  $\tau_B$  too much (the difference is  $\approx 10$  ps, which corresponds to  $\approx 5\%$ ). Taking into account the uncertainty in  $v_D$  which amounts approximately 10%, one can consider the dislocation density calculated from Eq. (1) as a reasonable estimation.

### 3.2 As-quenched Mg10Gd alloy

Only the reflections corresponding to the hexagonal Mg lattice were found in the XRD spectrum of as-quenched Mg10Gd alloy. The lattice parameters  $a = 0.32187(7)$  nm and  $c = 0.5212(1)$  nm were obtained from fit of the XRD data. A comparison with the lattice parameters of pure Mg [18] revealed that the lattice expansion due to a substitution of Gd atoms is not isotropic as expected from Vegard's rule for diluted solid solutions. There is a significant expansion of the  $a$  parameter (the relative increase  $\sim 0.29\%$  compared to pure Mg is higher than  $\sim 0.21\%$  estimated using Vegard's rule), while the  $c$  parameter remains practically unchanged (the relative increase is only  $\sim 0.03\%$  contrary to the  $\sim 0.17\%$  estimated from Vegard's rule). Thus, the  $c/a$  ratio in the Mg10Gd alloy is lowered much more (the relative decrease  $\sim 0.26\%$ ) than estimated using Vegard's rule ( $\sim 0.04\%$ ).

The as-quenched Mg10Gd specimen exhibits a two component PL spectrum, see Table 1. The shorter component with a dominant intensity represents a contribution of free positrons. In addition, a longer component with lifetime  $\tau_2 \approx 300$  ps was resolved in the PL spectrum. A typical TEM image of the as-quenched alloy is shown in Fig. 1. The as-quenched specimen is characterised by large coarse grains and

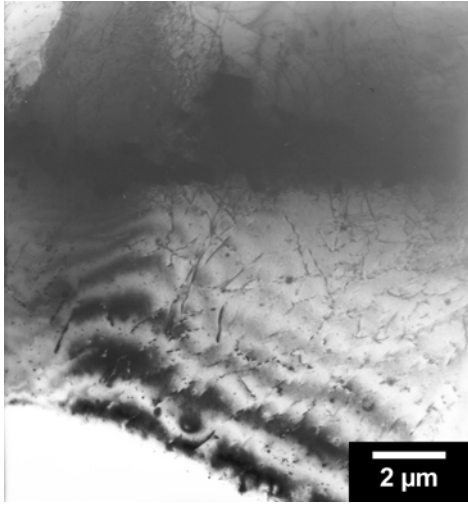


**Fig. 1** Bright-field TEM image of the as-quenched Mg10Gd specimen.

a low density of dislocations  $\rho_D < 10^{12} \text{ m}^{-2}$ , which approaches the lower sensitivity limit of PL spectroscopy [6]. Thus, positrons trapped at dislocations cannot make a significant contribution to the longer component. This conclusion is reinforced by the  $\tau_2$  value which is remarkable longer than 256 ps for dislocations in Mg (see Table 1) and indicates, therefore, positron trapping at another type of defects.

The calculated lifetimes  $\tau_v$  of positrons trapped in a vacancy in Mg10Gd alloy are shown in Table 2. The lattice parameters of Mg10Gd determined by XRD were used in the calculations. Two defect configurations in Mg10Gd alloy were considered: (i) a vacancy surrounded only by Mg atoms as the nearest neighbours and (ii) a vacancy–Gd pair, i.e. a vacancy with one Gd atom in the nearest neighbour position. The calculations revealed that the positron lifetime for a vacancy–Gd pair is about 6 ps shorter, see Table 2. It should be mentioned that no relaxation of atom positions was considered in the calculations. In order to estimate the influence of atom relaxation we calculated the positron lifetime for a vacancy–Gd pair with a Gd atom relaxed 10% towards the vacancy. Despite the fact that such a relaxation is too high and one would expect that the actual relaxation of Gd atom is much smaller, the calculated lifetime of trapped positrons is only about of 0.5 ps shorter than that of the non-relaxed configuration. Thus, the effect of atom relaxation on calculated positron lifetimes can be neglected in this case.

The experimental lifetime  $\tau_2$  measured in the as quenched Mg10Gd agrees well with the calculated lifetime  $\tau_v$  for a Mg monovacancy, see Table 2. Thus, we can attribute the second component to positrons trapped in the quenched-in vacancies. Taking into account the experimental error of 9 ps in the measured lifetime  $\tau_2$  (see Table 1), it is clear that the difference between a vacancy surrounded completely by Mg atoms and a vacancy–Gd pair is too small to distinguish by PL measurements between these two defect configurations. The quantity  $\tau_t^{\text{STM}}$  calculated from Eq. (2) agrees well with  $\tau_b$  testifying that the sample contains indeed homogeneously distributed defects of single type.

However, it is well known that vacancies in Mg become mobile well below room temperature [19]. As a consequence, thermal vacancies quickly disappear in a specimen quenched to room temperature. Hence, the vacancies present in the quenched Mg10Gd specimen must be stabilised by Gd atoms.

The equilibrium concentration of thermal vacancies at the homogenisation temperature  $T = 500 \text{ }^\circ\text{C}$  is

$$c_v^* = e^{S_v^F/k} e^{-E_v^F/kT}, \quad (3)$$

where  $S_v^F$  and  $E_v^F$  denote the vacancy formation entropy and energy, respectively. Using  $S_v^F \approx (2-3)k$  [20] and  $E_v^F = 0.83 \text{ eV}$  [21] we obtained  $c_v^* = (2.9-7.8) \times 10^{-5} \text{ at}^{-1}$ . The equilibrium concentration of vacancy–Gd pairs can be estimated from the expression

$$c_{v\text{-Gd}}^* = c_v^* c_{\text{Gd}}^* e^{E_{v\text{-Gd}}^B/kT}, \quad (4)$$

where  $c_{\text{Gd}} = 1.57 \times 10^{-2} \text{ at}^{-1}$  is the atomic concentration of dissolved Gd atoms in the specimen at the homogenisation temperature and  $E_{\text{v-Gd}}^{\text{B}}$  stands for the vacancy–Gd binding energy. The concentration  $c$  of quenched-in vacancies can be calculated from the PL results using the two state trapping model [6]

$$c = \frac{1}{\nu_{\text{v}}} \frac{I_2}{I_1} \left( \frac{1}{\tau_{\text{B}}} - \frac{1}{\tau_2} \right), \quad (5)$$

where the factor  $\nu_{\text{v}}$  is the specific positron trapping rate for a Mg monovacancy. In this work we used  $\nu_{\text{v}} = 1.1 \times 10^{13} \text{ at s}^{-1}$ , as published in [22]. Using this value, we obtain from Eq. (5)  $c = 6.2 \times 10^{-5} \text{ at}^{-1}$ , i.e. a concentration comparable with  $c_{\text{v}}^*$  at the homogenisation temperature. Clearly,  $c_{\text{v}}^*$  cannot be lower than  $c$ . Thus, we can refine our estimation of the equilibrium concentration of thermal vacancies at the homogenisation temperature given by Eq. (3) so that  $c_{\text{v}}^* = (6.2 - 7.8) \times 10^{-5} \text{ at}^{-1}$ . Assuming that the concentration of quenched-in vacancies bound to Gd atoms equals the equilibrium concentration of vacancy–Gd pairs at the homogenisation temperature, i.e.  $c = c_{\text{v-Gd}}^*$ , we can estimate from Eq. (4) the binding energy between a vacancy and a Gd atom:  $E_{\text{v-Gd}}^{\text{B}} = (0.26 - 0.28) \text{ eV}$ . It should be mentioned that  $\nu_{\text{v}}$  published in [22] is approximately one order of magnitude lower than typical  $\nu_{\text{v}}$  values in other metals. A small effect of positron trapping in Mg vacancies compared to the effect observed in other metals was found in PL measurements [23] as well as in Doppler broadening studies [24]. It indicates a low binding energy of a positron to a monovacancy in Mg [23]. This seems to be in sympathy with theoretical predictions of the strength of positron vacancy interaction [25].

CDB spectroscopy is sensitive to the local chemical environment of defects. The CDB ratio curve (with respect to the Mg reference specimen) for the well annealed pure Gd sample is plotted in Fig. 2. It exhibits a local maximum at  $8 \times 10^{-3} m_0 c$ , which comes from 5s and 5p Gd electrons, and another smaller local maximum at  $23 \times 10^{-3} m_0 c$  representing a contribution from 4d and 5p orbital. The CDB ratio curve for the as-quenched Mg10Gd specimen is plotted in Fig. 2 as well. One can see that it reproduces well some features of the CDB ratio profile for pure Gd, namely a local maximum at  $8 \times 10^{-3} m_0 c$ . Thus we can attribute it to a contribution of positrons annihilating with electrons from the electron shells of Gd atoms. The CDB ratio curve measured on the as-quenched Mg10Gd specimen can be reasonably approximated assuming  $\eta = 10\%$  fraction of positron annihilations with the Gd electrons plotted by the

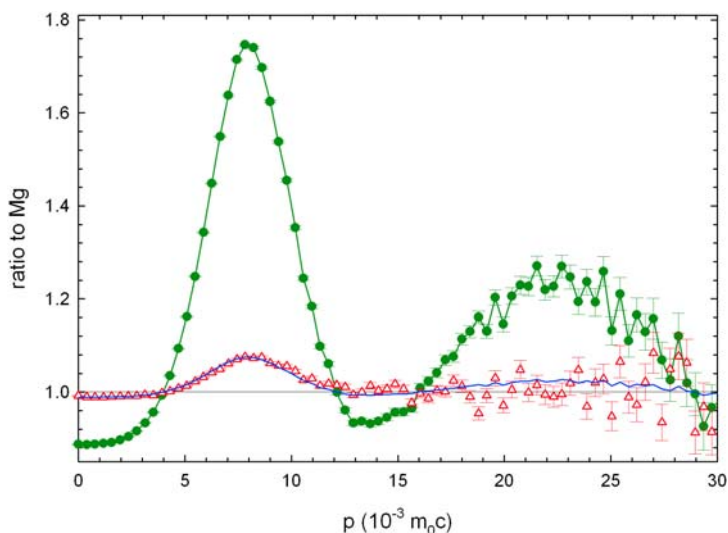


**Fig. 2** (online colour at: [www.pss-a.com](http://www.pss-a.com)) Experimental CDB ratio curves (with respect to the well annealed Mg): full green circles – well annealed pure Gd, open red circles – as-quenched Mg–10Gd sample. The  $\eta = 10\%$  fraction of positrons annihilated by Gd electrons (calculated from the CDB profile of pure Gd) is plotted as a solid blue line.

solid line in Fig. 2. The atomic concentration of Gd in the alloy studied is only 1.57 at%. A relatively high fraction  $\eta$  indicates, therefore, preferential positron annihilations with Gd electrons. The proton numbers for Gd and Mg atom, respectively, are  $Z = 64$  and  $Z = 12$ . Thus, Gd atom core exhibits approximately 5 times higher positive charge. As a consequence a free positron is strongly repelled from Gd atoms in Mg10Gd alloy. Relatively high fraction of positrons annihilating with Gd electrons cannot be, therefore, explained by annihilation of free positrons. It is reasonable to assume that fraction of free positrons annihilating with Gd electrons equals roughly to atomic concentration of Gd, i.e. it lies around 1.6%. The high fraction  $\eta$  observed in experiment can be explained by positron trapping in vacancies associated with Gd atoms. Vacancy represents a potential well for positron despite that fact that a Gd atom is placed in the nearest neighbour position. Presence of Gd attached to vacancy leads only to a slight reduction of positron binding energy. From calculations we obtained lowering of positron binding energy about of 0.2 eV. It can be seen also from very slight shortening of positron lifetime caused by presence of Gd atom attached to vacancy. Hence, positrons are trapped in vacancies associated with Gd atoms in similar way as in free vacancies surrounded completely by Mg atoms. The electron shell of a Gd atom consists of 64 electrons, while a Mg atom contains 12 electrons. Thus, probability that trapped positron annihilates with Gd electrons is roughly 5 times higher.

The fraction  $F_v$  of positrons annihilating from the trapped state in vacancies can be calculated using the two state STM [6]

$$F_v = \frac{\lambda_B}{\lambda_B + K_v}, \quad (6)$$

where  $K_v$  is the positron trapping rate to vacancies

$$K_v = \frac{I_2}{I_1} \left( \frac{1}{\tau_B} - \frac{1}{\tau_2} \right). \quad (7)$$

Using Eqs. (6) and (7) one obtains  $F_v = (13.6 \pm 0.8)\%$  for the as-quenched Mg10Gd alloy. There is 12 nearest neighbour positions around vacancy in the hcp structure, but probability that positron annihilates with Gd electron is 5 times higher than annihilation with Mg electron. Hence, the fraction of positrons, which are trapped and annihilates with Gd electrons is roughly  $F_v/3 \approx 5\%$ . The total fraction  $F$  of positrons annihilating with Gd electrons is a superposition of contribution of trapped positrons ( $\approx 5\%$ ) and free positrons ( $\approx 2\%$ ), i.e.  $F \approx 7\%$ . Although, this value is in order of magnitude comparable with the fraction  $\eta = 10\%$  measured by CDB, the estimated fraction  $F$  is slightly smaller. It indicates that position of Gd atom is most probably relaxed towards vacancy which leads to higher overlap of positron wave function with that of Gd electrons.

### 3.3 Thermal development of microstructure of Mg10Gd alloy

Microstructural development and precipitation effects in Mg10Gd alloy with increasing temperature are discussed in this section. PL spectra of Mg10Gd sample are best matched by two components at all the annealing temperatures (from 20 °C to 500 °C). The shorter component with a lifetime  $\tau_1$  and relative intensity  $I_1$  describes the contribution of free positrons, while the longer component with a lifetime  $\tau_2$  and intensity  $I_2$  arises from positrons trapped at defects. The defect component can vanish at some temperatures. The lifetime  $\tau_2$  of the defect component remains approximately constant with temperature indicating that the open volume of positron traps does not change. The temperature dependence of the relative intensity  $I_2$  of the defect component is plotted in Fig. 3. A map of the electron momentum distribution seen by positrons was measured by CDB (a ratio with respect to well-annealed Mg) at various annealing temperatures and is shown in Fig. 4. The CDB ratio curves for all annealing temperatures exhibit features typical for positron annihilation by Gd electrons. The fraction  $\eta$  of positrons annihilated by Gd electrons, obtained from the fit of the CDB ratio profiles measured at various annealing temperatures, is plotted in Fig. 3. Changes of macroscopic properties with temperature were monitored by measurements of micro-

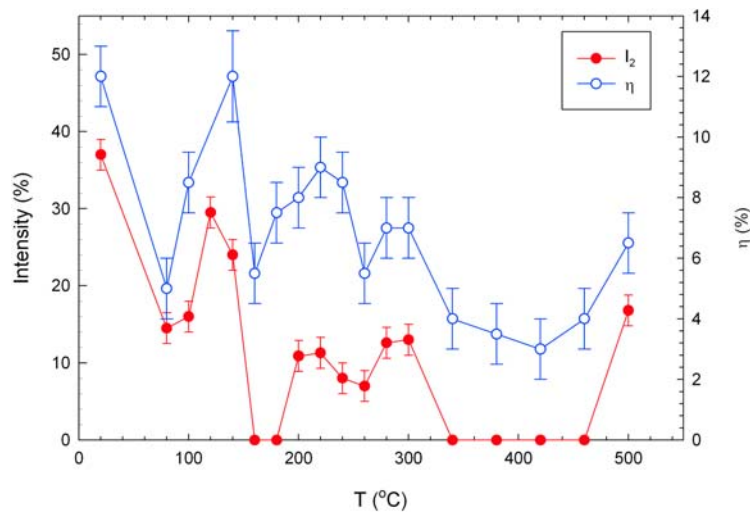


**Fig. 3** (online colour at: [www.pss-a.com](http://www.pss-a.com)) Temperature dependence of the relative intensity  $I_2$  of positrons trapped at defects (full red circles) and the fraction  $\eta$  of positrons annihilated by Gd electrons (open blue circles). The relative intensity  $I_2$  was obtained from a fit of PL spectra while the fraction  $\eta$  was measured by CDB.

hardness HV, which is plotted in Fig. 5 as a function of the annealing temperature. The temperature dependence of electrical resistivity for the Mg10Gd alloy isochronally annealed using the same procedure as in our work, was measured by Vostry et al. [4]. The relative changes of electrical resistivity as a function of temperature are also plotted in Fig. 5.

A decrease in  $I_2$  was observed in the sample annealed at 80 °C, see Fig. 3. It indicates that some quenched-in vacancies associated with Gd atoms were annealed out. This is substantiated also by a decrease in  $\eta$  due to a smaller fraction of positrons annihilating from the trapped state in vacancy–Gd pairs.

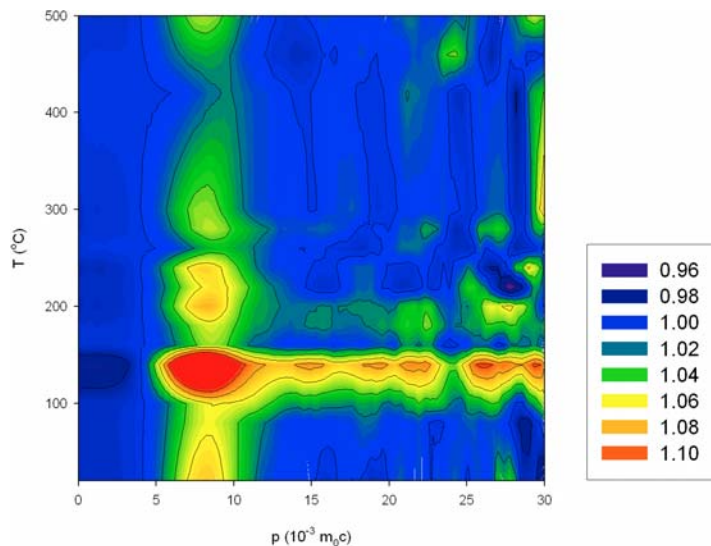


**Fig. 4** (online colour at: [www.pss-a.com](http://www.pss-a.com)) A map of electron momentum distribution (ratio with respect to well annealed Mg) measured by CDB on the Mg10Gd alloy at various annealing temperatures. The CDB ratio curves were appropriately smoothed using the Savitzky–Golay smoothing filter.

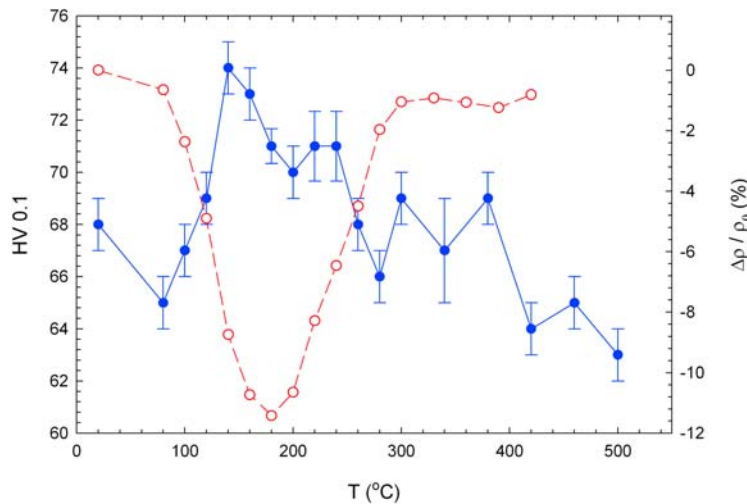


**Fig. 5** (online colour at: [www.pss-a.com](http://www.pss-a.com)) Temperature dependence of microhardness HV 0.1 (full blue circles) and the relative change in electrical resistivity  $\Delta\rho/\rho_0$  (open red circles).

Above 100 °C,  $I_2$  starts to increase again indicating an increase in defect density. The increase of  $I_2$  is accompanied by an increase in  $\eta$  and microhardness, see Figs. 3 and 5. Such a behaviour can be explained by clustering of dissolved Gd atoms, which indicates pre-precipitation of the  $\beta''$  phase precipitates formed at higher temperatures. The electron diffraction patterns of Mg10Gd alloy annealed up to 180 °C is shown in Fig. 6. One can see diffuse diffraction spots from  $D0_{19}$  particles in the figure. It confirms the existence of very fine  $\beta''$  phase precipitates with the  $D0_{19}$  hexagonal structure as was observed also in [4]. One can assume that Gd-rich clusters are formed at the early stages of the  $\beta''$  phase precipitation. The Gd-rich clusters or small particles are associated with vacancy like defects, which are trapping sites for positrons. A similar effect, i.e. the formation of small Sn clusters associated with vacancy like defects, was observed recently in an Al–Sn alloy [26]. A higher concentration of defects in Mg10Gd sample leads to the observed increase in intensity  $I_2$  of trapped positrons. The fact that these defects are associated with Gd atoms is reflected by the increase in the fraction  $\eta$  of positrons being annihilated by Gd electrons. Note that the electrical resistivity of isochronally annealed Mg10Gd alloy also starts to decrease from 100 °C, see Fig. 5. This supports our interpretation that precipitation effects in Mg10Gd alloy begin by formation of Gd-rich clusters starting at this temperature. Precipitation of  $\beta''$  phase particles (and their precursors) causes an indispensable hardening, as demonstrated by an increase in microhardness in the temperature range from 100 °C to 140 °C. The specimen exhibits a maximum microhardness at 140 °C and the relative increase in HV with respect to the as-quenched specimen is  $\approx 10\%$ . A local maximum of  $I_2$  and  $\eta$  can be seen at temperatures 120 °C and 140 °C, respectively. Precipitation of the  $\beta''$  phase particles can be seen clearly also on the map of the electron density (Fig. 4) by the peak at  $p = 8 \times 10^{-3} m_0c$  occurring at 140 °C. At higher temperatures a coarsening of the  $\beta''$  phase precipitates occurs. This leads to an increase in the mutual distance of the precipitates, which reduces the probability of positron trapping. Moreover, the defects created in the early stages of precipitation are annealed out. Both these effects are reflected by a decrease in  $I_2$  and  $\eta$ , see Fig. 3. Electrical resistivity exhibits a local minimum attributed to the  $\beta''$  phase at 180 °C, see Fig. 5 and 6. In Fig. 3 we can see that the defect component vanished ( $I_2 = 0$ ) at that temperature. Similarly  $\eta$  exhibits a local minimum at 160 °C. Note that  $\eta$  lies above zero at all temperatures due to a contribution of free positrons being annihilated by electrons from the electron shells of Gd atoms dissolved in Mg matrix.

Further annealing at temperatures above 160 °C leads to a partial dissolution of the  $\beta''$  phase particles and to precipitation of a semicoherent  $c$ -base centred orthorhombic ( $c$ -bco)  $\beta'$  phase. The orientation relationship of the  $\beta'$  phase  $[0001]_{\text{Mg}} \parallel [001]_{c\text{-bco}}$  and  $\{2\bar{1}\bar{1}0\}_{\text{Mg}} \parallel (100)_{c\text{-bco}}$  was found by TEM in

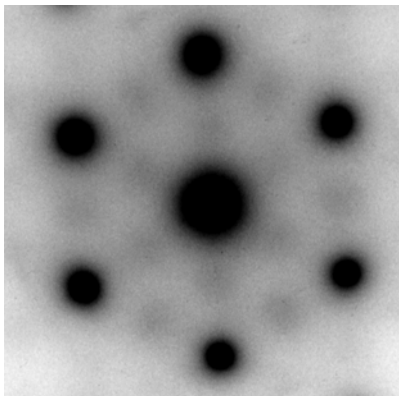


**Fig. 6** [0001] diffraction patterns of the  $\alpha'$ -Mg and the  $D0_{19}$  phases in Mg10Gd annealed up to 180 °C. Diffuse  $\{10\bar{1}0\}$  reflections of the  $D0_{19}$  phase are in the middle between those of the  $\alpha'$ -Mg matrix.

Mg–15wt%Gd alloy [4]. All three possible orientation relationship modes of  $\beta'$  phase precipitated as plates on the  $\{2\bar{1}10\}$  matrix plane were observed [4]. Open-volume misfit defects are present at the  $\beta'$  phase particle matrix interface where the coherence with the matrix is lost, i.e. in directions parallel to the  $\{2\bar{1}10\}$  matrix plane. The misfit defects are trapping sites for positrons with an open volume comparable to that of vacancy. As a consequence the  $\beta'$  phase precipitation causes an increase in  $I_2$ , see Fig. 3. As the misfit defects are associated with Gd-rich  $\beta'$  phase particles, the trapped positrons are annihilated in the vicinity of the Gd atoms. This leads to increasing fraction  $\eta$  of positrons being annihilated by Gd electrons, see Fig. 3. The increased values of  $I_2$  can be seen in the temperature range from 200 °C to 300 °C. It corresponds well with enhanced values of  $\eta$  in that temperature interval as well as a wider peak being observed in the map of the electron density in Fig. 4. It should be noted that contrary to the Mg–15 wt% Gd alloy, particles of the  $\beta'$  phase were not directly observed by the TEM in Mg10Gd [4]. Only slight change in the shape of resistivity annealing curve of Mg10Gd was detected at the same temperature where  $\beta'$  phase precipitation was observed in Mg–15wt%Gd alloy [4]. It indicates that the volume fraction of  $\beta'$  phase precipitates is rather small. Due to the very high sensitivity of PAS to open volume defects the  $\beta'$  phase formation was also verified in the Mg10Gd alloy. Note that a very similar effect, i.e. an increase of concentration of positron trapping sites due to the formation of semicoherent precipitates, was also observed in the case of  $\beta'$  phase precipitation in Al–Cu alloy [27].

There appears to be a localised drop in  $I_2$  and  $\eta$  in temperature interval from 240 °C to 260 °C, see Fig. 3. It is known from TEM and electrical resistivity measurements [4] that dissolution of two of the  $\beta'$  phase orientation modes takes place in Mg–15wt%Gd alloy, whereas the particles of the remaining mode grow into oval plates with a diameter of about 100 nm [4]. Similar behaviour can also be expected in Mg10Gd alloy. The variation in defect density connected with dissolution of the two  $\beta'$  phase orientation modes could be responsible for the localised drop in  $I_2$  and  $\eta$ . However, taking into account the experimental errors one cannot exclude the possibility that it is only a random fluctuation. It should be noted that the decrease in microhardness ceased in the temperature range from 200 °C to 240 °C, see Fig. 5, obviously due to the formation of  $\beta'$  phase particles. However at higher temperatures HV decreases, which can be explained by the dissolution of the two  $\beta'$  phase orientation modes.

Further annealing up to temperatures higher than 300 °C leads to a decrease in  $\eta$  and the disappearance of the defect component with intensity  $I_2$  (see Fig. 3) due to dissolution of  $\beta'$  phase precipitates. The Mg10Gd specimen exhibits only a single component PL spectrum in the temperature range from 340 °C to 460 °C, i.e. virtually all positrons annihilate freely and positron trapping at defects is negligible. Dissolution of the  $\beta'$  phase particles is reflected also by a decrease in HV in this temperature range, see Fig. 5. Note that the formation of the stable  $\beta$  phase ( $Mg_5Gd$ , fcc structure) was found in the Mg–15wt%Gd alloy annealed at higher temperatures [4]. It is reflected by a local minimum in the electrical resistivity at 420 °C [4]. The  $\beta$  phase particles are not coherent with Mg matrix. Therefore, one can expect that misfit defects are present at the  $\beta$  phase precipitate-matrix interface. However, TEM studies of Mg–15wt%Gd revealed that the  $\beta$  phase precipitates as large plates lying parallel to the  $\{10\bar{1}0\}$  planes of

the Mg matrix. It is energetically favourable because the misfit in this plane is small. Thus, open-volume misfit defects capable of positron trapping are expected only to be present at the edges of the plate-shaped  $\beta$  phase precipitates. Significantly larger sized  $\beta$  phase precipitates result in a substantially lower fractional area of the edges compared to the fine  $\beta'$  phase precipitates. The distance between the coarse  $\beta$  phase particles also becomes greater. Moreover, the volume fraction of the  $\beta$  phase precipitates is lower because the higher temperature leads to increased solubility of Gd in Mg matrix. All these factors result in a lower volume fraction of the misfit defects and thereby to a reduced positron trapping compared to the  $\beta'$  phase precipitates. Indeed, no changes in  $I_2$  and  $\eta$  which could be interpreted by the formation of  $\beta$  phase particles took place in the Mg10Gd alloy studied in the present work. This indicates that the concentration of the misfit defects is too low to be detected by PAS.

The solid solution of Gd in Mg is restored in the Mg10Gd specimen by annealing above 460 °C. Analogous to the homogenisation annealing the thermal vacancies become associated with diluted Gd atoms and vacancy–Gd pairs are formed. The thermal vacancies not associated with Gd atoms disappeared quickly after quenching the annealed specimen to room temperature. Thus, only those vacancies bound to Gd atoms remain in the specimen quenched to room temperature. Positron trapping in the vacancy–Gd pairs is apparent by an increase in  $\eta$  as well as by the appearance of the defect component with the intensity  $I_2$  at 500 °C, see Fig. 3. The intensity  $I_2$ , in addition to the fraction  $\eta$  of the specimen annealed at 500 °C, are slightly lower than that of the homogenized material. This is probably due to incomplete dissolution of Gd because of the shorter annealing time (30 min annealing versus 6 h homogenisation).

#### 4 Conclusion

Thermal development of microstructural and precipitation effects in Mg10Gd alloy were studied by PAS combined with XRD and microhardness measurements. Vacancies bound to Gd atoms are present in the homogenized specimen quenched to room temperature. Subsequent isochronal annealing leads initially to clustering of Gd atoms followed by the formation of fine coherent precipitates of the  $\beta''$  phase, which produces a significant hardening. Further annealing at higher temperatures leads to the formation of the semicoherent  $\beta'$  phase particles containing open volume misfit defects in precipitate–matrix interfaces where the coherence was lost. Precipitation of the  $\beta$  phase at higher temperatures could not be detected by PAS. A good correlation between the intensity  $I_2$  of positrons trapped at defects and the  $\eta$  fraction of positrons being annihilated by Gd electrons provides evidence for the enhanced concentration of Gd in the local environment of the defects.

**Acknowledgements** Financial support from The Czech Science Foundation (contract 106/05/0073) and The Ministry of Education, Youth and Sports of Czech Republics (project MS 0021620834) are highly acknowledged.

#### References

- [1] B. L. Mordike, Mater. Sci. Eng. A **324**, 103 (2002).
- [2] T. B. Massalski, Binary Alloy Phase Diagrams, Vol. 3 (ASM International, Materials Park, OH, 1990).
- [3] S. Kamado, S. Iwasawa, K. Ohuchi, Y. Kojima, and R. Ninomiya, J. Jpn. Inst. Light Met. **42**, 727 (1992).
- [4] P. Vostrý, B. Smola, I. Stulíková, F. von Buch, and B. L. Mordike, phys. stat. sol. (a) **175**, 491 (1999).
- [5] P. Hautojärvi and A. Vehanen, in: Positrons in Solids. Topics in Current Physics Vol. 12, edited by P. Hautojärvi (ed.) (Springer-Verlag, Berlin, 1979), p. 1.
- [6] P. Hautojärvi and C. Corbel, in: Positron Spectroscopy of Solids, Proceedings of The International School of Physics “Enrico Fermi”, edited by A. Dupasquier and A. P. Mills, Vol. LXXXIII (IOS Press, Amsterdam, 1995), p. 491.
- [7] K. G. Lynn, J. R. MacDonald, R. A. Boie, L. C. Feldman, J. D. Gabbe, M. F. Robbins, E. Bonderup, and J. Golochenko, Phys. Rev. Lett. **38**, 241 (1977).
- [8] F. Bečvář, J. Čížek, and I. Procházka, Acta Phys. Pol. A **95**, 448 (1999).
- [9] F. Bečvář, J. Čížek, L. Lešták, I. Novotný, I. Procházka, and F. Šebesta, Nucl. Instrum. Methods **443**, 557 (2000).
- [10] I. Procházka, I. Novotný, and F. Bečvář, Mater. Sci. Forum **255–257**, 772 (1997).

- [11] M. J. Puska and R. M. Nieminen, *J. Phys. F, Met. Phys.* **13**, 333 (1983).
- [12] A. P. Seitsonen, M. J. Puska, and R. M. Nieminen, *Phys. Rev. B* **51**, 14057 (1995).
- [13] E. Boroński and R. M. Nieminen, *Phys. Rev. B* **34**, 3820 (1986).
- [14] E. Dryzek, J. Kuriplach, and J. Dryzek, *J. Phys.: Condens. Matter* **10**, 6573 (1998).
- [15] L. C. Smedskjaer, M. Manninen, and M. J. Fluss, *J. Phys. F, Met. Phys.* **10**, 2237 (1980).
- [16] M. Abdelrahman and E. Badawi, *Jpn. J. Appl. Phys.* **35**, 4728 (1996).
- [17] J. Čížek, I. Procházka, M. Cieslar, R. Kužel, J. Kuriplach, F. Chmelík, I. Stulíková, F. Bečvář, O. Melikhova, and R. K. Islamgaliev, *Phys. Rev. B* **65**, 094106 (2002).
- [18] PDF-2, Powder diffraction pattern database, ICDD (International Center for Diffraction Data), record number 35-0821.
- [19] P. Tzanetakis, J. Hillairet, and G. Revel, *phys. stat. sol. (b)* **75**, 433 (1976).
- [20] H. Wollenberger, in: *Physical Metallurgy*, edited by R. Cahn and P. Haasen, Vol. 2 (North-Holland, Amsterdam, 1983), p. 1146.
- [21] H. Krimmel and M. Fähnle, *Phys. Rev. B* **62**, 5489 (2000).
- [22] G. M. Hood, *Phys. Rev. B* **26**, 1036 (1982).
- [23] P. Hautojärvi, J. Johansson, A. Vehanen, and J. Yli-Kauppila, *Appl. Phys. A, Solids Surf.* **27**, 49 (1982).
- [24] D. Segers, M. Dorikens, and L. Dorikens-Vanpraet, *Solid State Commun.* **36**, 943 (1980).
- [25] M. Manninen, R. Nieminen, P. Hautojärvi, and J. Arponen, *Phys. Rev. B* **12**, 4012 (1975).
- [26] J. Čížek, O. Melikhova, I. Procházka, J. Kuriplach, I. Stulíková, P. Vostrý, and J. Faltus, *Phys. Rev. B* **71**, 064106 (2005).
- [27] O. Melikhova, J. Čížek, I. Procházka, J. Kuriplach, I. Stulíková, and J. Faltus, *Mater. Struct.* **8**, 61 (2001).